UNDER-RESOLVED DIRECT NUMERICAL SIMULATION OF NACA0012 AT STALL

Mohsen Lahooti[1*], Guglielmo Vivarelli[2], Francesco Montomoli[3] and Spencer J. Sherwin[4]

[1,2,3] Imperial College, SW7 2AZ London, United Kingdom

[1] m.lahooti@imperial.ac.uk, [2] guglielmo.vivarelli12@imperial.ac.uk,
[3] f.montomoli@imperial.ac.uk, [4] s.sherwin@imperial.ac.uk

Key words: Turbulence Transition, Flow Separation, Stall, Direct Numerical Simulation, High-Order Methods, NACA0012

Abstract. In this work a high-order *spectral-h/p* element solver is employed to efficiently but accurately resolve the flow field around the *NACA*0012 aerofoil. In particular, the conditions considered are a *Reynolds number* of 150000 and three angles of attack, namely $9°$, $10°$ and $12°$. This particular study aims at providing the necessary preliminary insight into the flow dynamics of the turbulent transition at near-post stall with very well resolved *Large Eddy Simulation* range if not *Direct Numerical Simulation*. Therefore, the first step consists of determining the mesh resolution required and the spanwise length. Our results repeatedly demonstrate the possible existence of a large-scale low-frequency 2D dominant flow structure over the span where. It was found that employing a single chord length in z is not sufficient to capture it.
Concerning the flow behaviour, it is observed that a laminar separation bubble forms at the aerofoil leading edge. This tends to move upstream, shorten in length and increase in height as the angle of attack is increased. Mild three-dimensional behaviour is seen right from the beginning of the aerofoil suction surface with turbulent transition occurring just after the re-attachment point. In particular, this is seen to happen sooner with higher aerofoil inclination. Finally, our results indicate an interaction of large-scale structures with the boundary layer.

1 INTRODUCTION

In this study, a high-fidelity numerical simulation is reported to reveal the key flow dynamics near post-stall regime of the *NACA*0012 aerofoil section at a *Reynolds number* (Re) of 1.5×10^5. This focuses on the separation bubble and laminar-to-turbulent transition. There are numerous works on the stall regime, but most of them concentrate on integral quantities such as aerodynamic coefficients[1;2]. Further, studies reporting flow dynamics details generally deal with low *Reynolds numbers*. For example, Zakaria et al.[3] investigated the flow over the *NACA*0012 at high angles of attack (α) with $Re = 7.99 \times 10^4$ using both experimental and computational tools. The main analysis concentrated on the vortex shedding characteristics from the *trailing edge* (*TE*). Eljack et al.[4] presented a detailed study of the flow and laminar separation bubble over various α values, enveloping the the onset of stall. However, the authors only considered
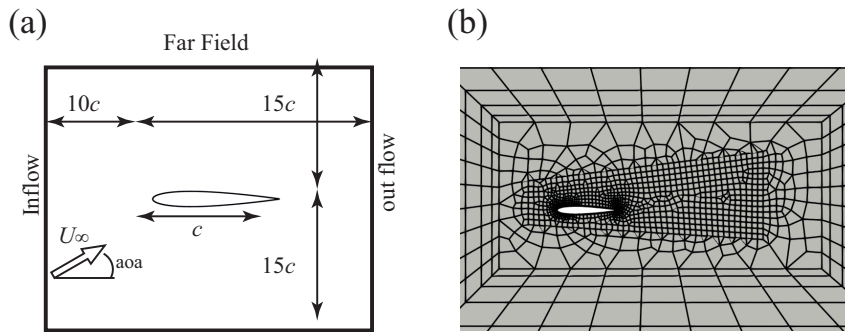
Figure 1: $NACA$0012 grid: zoom around the aerofoil.

two low *Reynolds numbers* equal to 5×10^4 and 9×10^4. Additionally, the flow conditions in their work were slightly compressible at $M = 0.4$ and had variable temperature and viscosity. Similarly, Rosti et al.[5] conducted a *Direct Numerical Simulation* (*DNS*) study of the $NACA$0012. Despite the detailed flow field analysis, the study only covered $Re \leq 5 \times 10^4$. Finally and more recently, Poels et al.[6] experimentally investigated and presented a detailed flow field for a range of $Re \leq 1.2 \times 10^5$. However, their study was limited to angles of attack less than 8°.

In the present study, a higher *Reynolds number* of $Re = 1.5 \times 10^5$ is considered which is in a more practical range of *High-Altitude Low-Endurance* (*HALE*) aero vehicles as well as vertical-axis wind turbines. Additionally, aiming to understand the transition mechanism near the post-stall, three angles of attack are considered corresponding to near pre-stall, near maximum-lift and near post-stall regimes, respectively. Details of the flow dynamics, separation, bubble and distribution of shear stress are studied over these angles and are reported in the results and discussion section.

2 PROBLEM DEFINITION AND NUMERICAL METHOD

The problem consists of turbulent flow over the well-known symmetric $NACA$0012 at $Re = 1.5 \times 10^5$ at three angles of attack equal to $\alpha = 9°$, $10°$ and $\alpha = 12°$. These correspond to near pre-stall, maximum lift and near post-stall. Turbulent simulations are conducted by solving the isothermal incompressible *Navier-Stokes* equations, where an *implicit Large-Eddy Simulation* (*iLES*), also known as *under-resolved Direct Numerical Simulation* (*uDNS*), approach is used for resolving the turbulent flow. A quasi-3D method is used for the simulations where the flow is assumed to be homogeneous in the spanwise direction with the spanwise length $L_z = c$, where c is the aerofoil chord length. Using the quasi-3D approach, the domain is discretized using high-order elements in the xy domain and *Fourier* planes in spanwise length. The schematic of the 2D xy surface together with the boundary conditions are shown in figure 1(a). The mesh was generated using $GMSH$[7] and converted to high-order elements with the $Nektar++$'s mesh generator *NekMesh*. Each *Fourier* plane, i.e. the xy domain, is tessellated using 2400 macro-elements. In each of these the flow variables are approximated using polynomial expansions of order $\mathscr{P} = 12$. Further, the boundary layer mesh consists of 6 layers of quadrilaterals with the first layer located at a height of $H_w = 1 \times 10^{-3}$ off the wall (in non-dimensional units). This wall distance together with polynomial order $\mathscr{P} = 12$ results in an actual first-layer wall
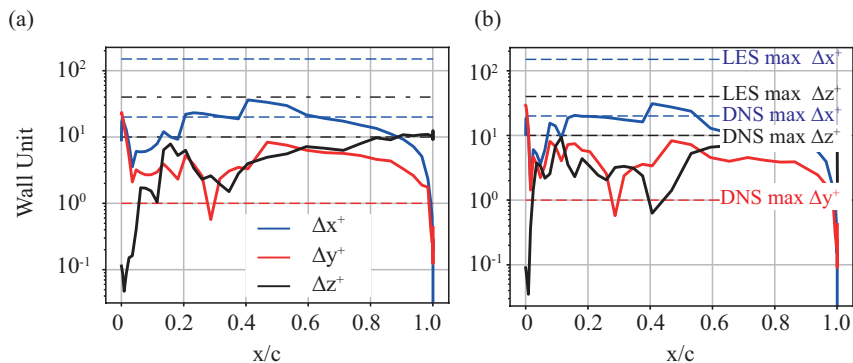
Figure 2: Near-wall grid spacing for (a) $\alpha = 9°$ (b) $\alpha = 12°$. The dashed lines represent the maximum acceptable values for *LES* and *DNS* simulations.

distance equal to $h_w = H_w/\mathcal{P} = 8.33 \times 10^{-5}$. On the other hand, the spanwise length L_z is discretized using 64 complex *Fourier* modes (128 *Fourier* planes). This, coupled with the xy-surface discretization results in approximately $40M$ degrees of freedom for each variable. The mesh resolution, particularly near the wall, is fine enough for *iLES* simulations. The values of Δx^+, Δy^+ and Δz^+ for the cases with $\alpha = 9°$ and $\alpha = 12°$ are shown in Fig. 2(a) and Fig. 2(b), respectively. As may be seen, the wall-normal distance Δy^+ is higher than the *LES/DNS* limit, but on average is about $\Delta y^+ = 5$ with a maximum of 10 for a limited number of points, mainly near the *leading edge* (*LE*) and mid-chord positions. Except for a limited region halfway along the chord, Δx^+ is within the *DNS* limit. Concerning the spanwise distance Δz^+, most of the near-wall spacing is appropriate to meet *DNS* requirements. Finally, a zoomed view of the macro-elements near the aerofoil is also depicted in figure 1(b). In all cases simulations are performed using a dimensionless time-step $\Delta t = 1 \times 10^{-5}$ until the solution reaches the $t^* = tU_\infty/c = 50$.

2.1 High-order spectral/hp element Nektar++ framework

Our simulations are conducted using the Nektar++[8;9] framework: this is a high-order *spectral-h/p element* implementation of the *Navier-Stokes* equations. This is an open-source suite of tools developed in *C++* for rapid development of high-order codes to solve partial differential equations. The *spectral-h/p element*[10] method allows both the flexibility of *h*-type discretizations, where *h* is the element size, as well as the exponential convergence of high-order methods using polynomial expansions of an arbitrary order $\mathcal{P}$ within each element.

The *Navier-Stokes* solver of the Nektar++ framework uses a stiffly stable high-order splitting scheme[11] for the velocity-pressure coupling and supports various time-integration schemes. In particular, the second-order implicit-explicit discretization is used in this work. The solver features the quasi-3D capabilities previously mentioned in Sec. 2 and supports various stabilization approaches. In the present work, a recently implemented stabilization method called *Gradient Jump Penalisation*[12] is employed to avoid numerical instability during the solution. For the theoretical aspects of the *spectral/hp element* method see Karniadakis and Sherwin[13], while implementation details and features of the Nektar++ framework can be found in Cantwell et al.[8]; Moxey et al.[9]
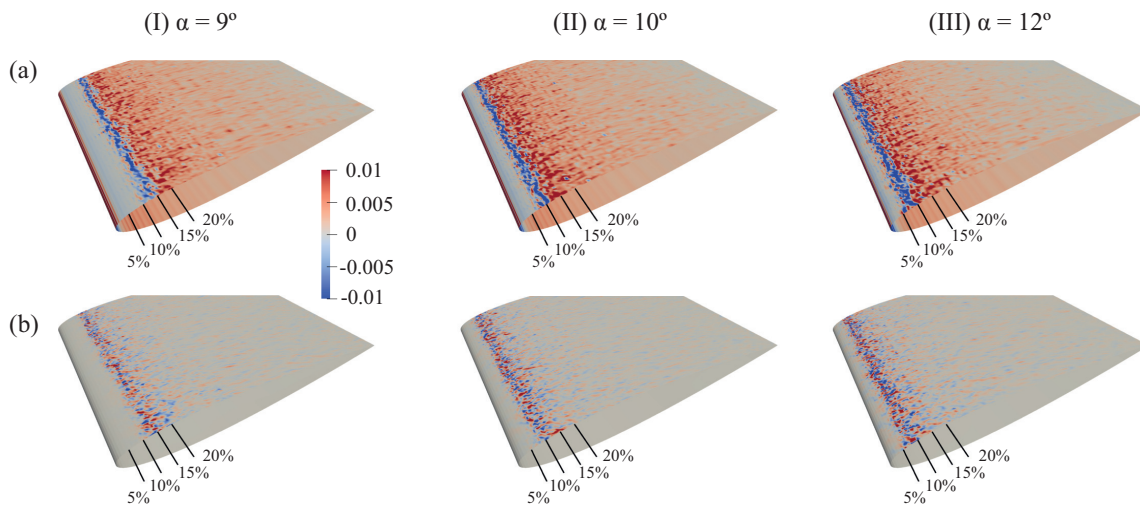
Figure 3: Instantaneous wall shear stress for flow at angles of attack $\alpha = 9°$, $10°$ and $12°$. (a) τ_{xx} (b) τ_{zz}.

3   RESULTS AND DISCUSSION

3.1   Flow Separation

The main focus of this work reverts around the flow behaviour on the suction surface of the aerofoil. In fact, flow features are very limited on the pressure side. Apart from the stagnation point moving further downstream as α is increased, the boundary layer along it remains laminar. On the upper surface, instead, very close to the LE, the flow separates, the location of it being a function of the angle of attack. The higher this is, sooner will separation occur. This is visible in the instantaneous axial wall shear stress as shown in Fig. 3(a) for all angles of attack considered. As evident from it, the separation starts with a low negative magnitude region of τ_{xx} (the gray area near the LE). This is then followed by a strip of stronger negative τ_{xx} (the blue strip in Fig. 3(a)) where small spots of positive shear are also present. After this region, the axial shear stress is almost entirely positive (red parts in Fig. 3(a)). This pattern suggests the formation of a separation bubble and a re-circulation zone close to the leading edge. The extent of this behaviour is highly dependent on the angle of attack and shrinks as the aerofoil is tilted further. To have a better view of this separation bubble, the dimensionless streamwise velocity (u^* field for each angle is reported in Fig. 4 for all angles. The separation bubble is clearly visible and corresponds to the blue contour zone: its length is approximately marked by the green arrows. From close inspection, it is obvious that as the aerofoil is tilted further from $\alpha = 9°$ [Fig. 4(a)], to $\alpha = 10°$ [Fig. 4(b)] and finally $\alpha = 12°$ [Fig. 4(c)], the bubble length reduces. On the other hand, its height grows. This behaviour results in the increase of acceleration of the air above it. This corresponds to the darker red patches above the blue recirculating region visible in Fig. 4.

To have a better insight of the flow dynamics of the separation bubble and its interaction with the flow, figure 5 reports the instantaneous and time-averaged axial wall shear stress at $\alpha = 9°$. The end of the separation bubble can be considered to be the marked by the first dashed line A: this corresponds to the lighter negative shear-stress region. The second region
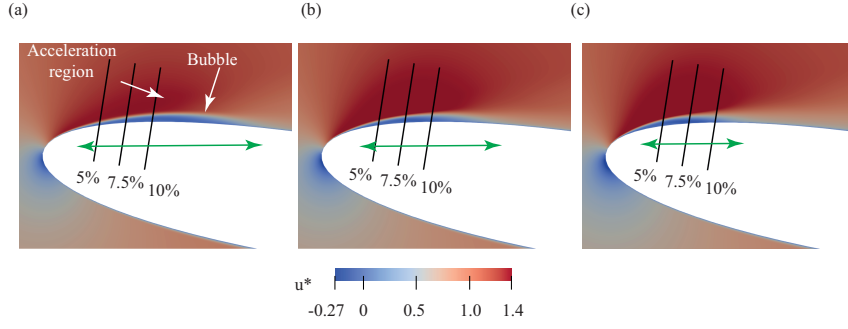
Figure 4: Time-averaged axial velocity contours and re-circulation bubble near the *LE* for (a) $\alpha = 9°$ (b) $\alpha = 10°$ and (c) $\alpha = 12°$. Note the percentages shown relate to chord positions.
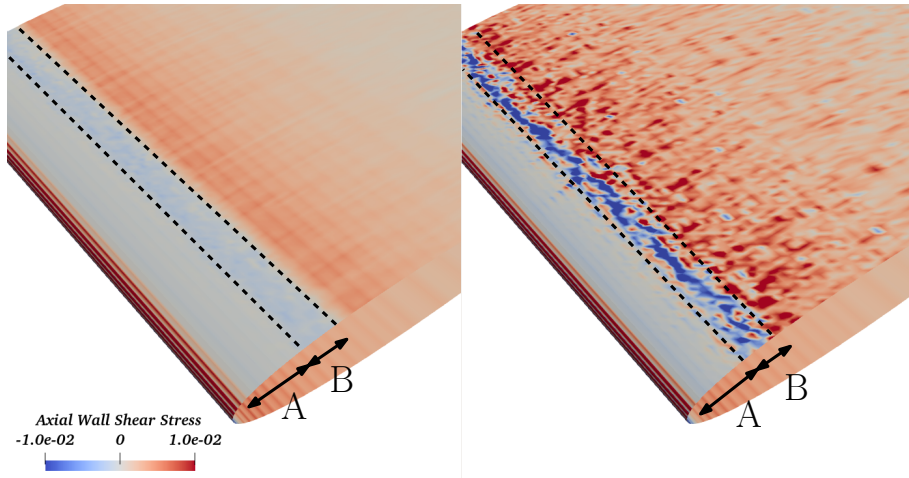

Figure 5: Time-averaged (left) and instantaneous (right) axial wall shear stress with approximate sketches of the bubble and transition region lengths.

enveloped by the two dashed lines A-B is the transition region. In the instantaneous case, this is characterised by high-intensity small and larger positive and negative pockets of shear stress, respectively.

An interesting observation is that the boundary layer thickness is almost identical for all cases when $x/c \leq 0.35$. This despite the change in location of the separation and height of the re-circulation bubble as α varies. This particular behaviour is shown in Fig. 6(a). The predicted boundary layer thickness remains close with at most $1\%c$ difference for $\alpha = 9°$ and $\alpha = 12°$ over the rest of the chord length. On the other hand, at $\alpha = 10°$, that also corresponds to the maximum lift conditions, there is a visible boundary layer height reduction. This can be related to some turbulent structures forming around the mid-chord for this particular angle of attack and further investigation is required to gain the necessary insight. As the flow conditions are incompressible, the approach described by Griffin et al.[14] was employed to determine the boundary layer height. This considers the total pressure asymptotic behaviour in the wall normal
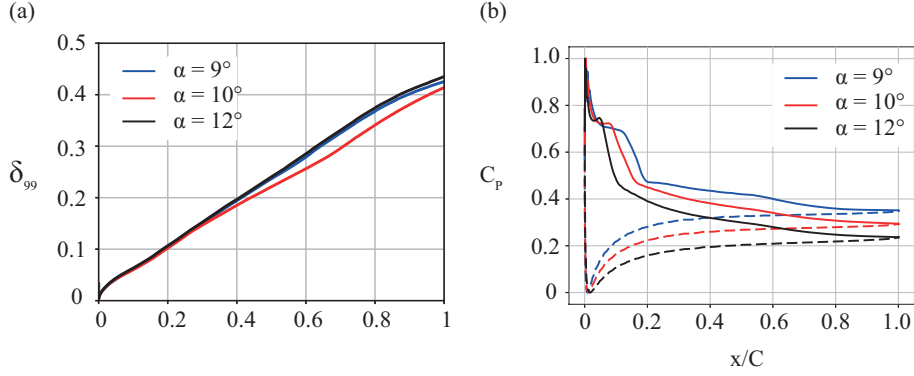
Figure 6: Comparison of (a) Boundary layer thickness and (b) Pressure Coefficient C_p for various angles of attack.
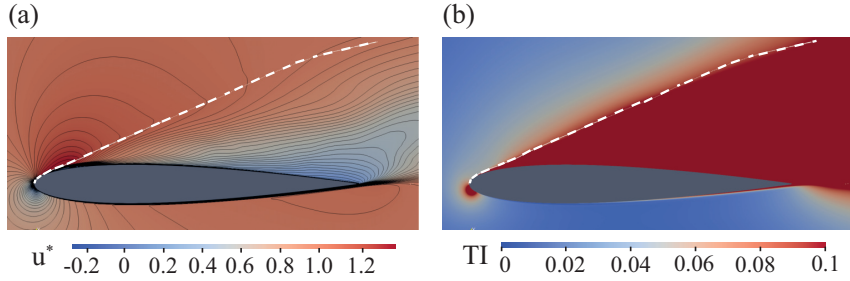

Figure 7: Predicted boundary layer height at $\alpha = 9°$ compiled over the contours of (a) dimensionless axial velocity u_x^* (b) Turbulent Intensity (TI%)

direction to recover a local reference velocity. To validate our estimation of δ_{99} (boundary layer thickness), Fig 7 is included. In particular, Fig. 7(a) compares the predicted quantity against contours of streamwise velocity, while Fig. 7(b) does so against the *turbulent intensity (TI)*. Clearly, the δ_{99} line cuts through the change in curvature of the u^* contour lines. Moreover, looking at the *turbulence intensity*, it may be seen how the line approximately follows the end of the region where $TI > 1\%$. Therefore, it may be concluded that the methodology is approximating the boundary layer height relatively well.

The separation bubble size could also be seen in the pressure coefficient (Fig. 6(b)). For $\alpha = 9°$, C_p has a peak of $\simeq 0.95$ around the LE region. This is followed by a sharp drop of $C_p \simeq .75$ at $x/c \simeq 0.05$ and continues to reduce with a very small slope till $x/c \simeq 0.15$. At this point, the trend has almost flattened out. After this, there is another abrupt vertical reduction to $C_p \simeq 0.5$ within the $0.15 < x/c < 0.2$ interval. This is consistent with the location of the bubble re-attachment and what was seen in the wall shear stress distribution (i.e the end of the negative τ_{xx} at $x/c \sim 0.15$ in Fig. 3(a)). As α is changed to $10°$ and then $12°$, the pressure coefficient increases to one at the aerofoil LE, suggesting separation is occurring here. Both C_p profiles have the same trend as for $\alpha = 9°$ but the extent of the flat plateau shrinks to $x/c \simeq 0.1$ and $x/c \simeq 0.75$, for $\alpha = 10°$ and $\alpha = 12°$, respectively. This is again consistent with what was
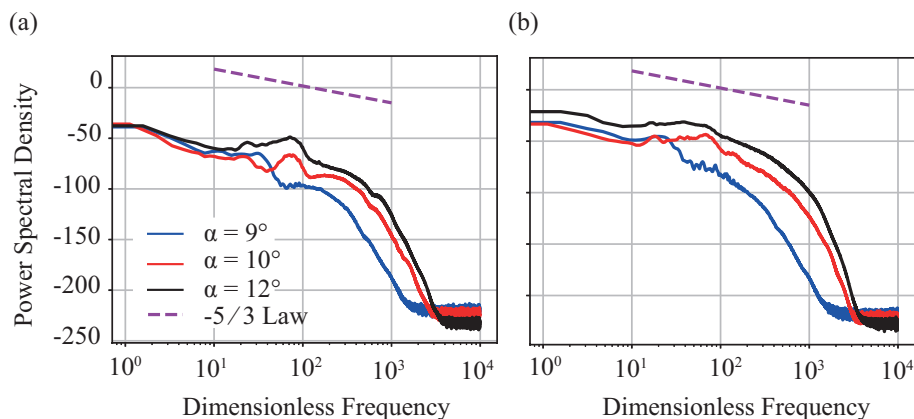
6

Figure 8: Power Spectral Density of axial velocity at (a) $x/c = 0.046$ (b) $x/c = 0.061$

previously discussed concerning the shear stress.

To further deepen our understanding of re-circulation region, two sampling points where placed within the shear layer between the accelerating flow and bubble. The *power-spectral density* (*PSD*) at the different aerofoil inclinations is reported in Fig. 8. Both locations show the presence of relatively wide-band peaks of similar frequency and magnitude. Although these low-frequency peaks indicate the presence of slow-dynamic structures in the flow, at the moment it is not clear whether these are induced by instabilities or large-scale low frequency structures forming over the span of the aerofoil.

The spanwise correlation of the fluctuating velocity components are computed using Eq.(1) and shown in Fig. 9 for all three angles of attack at $x/c = 0.046, 0.061, 0.1$ and 0.2 along the chord. These are necessary to understand whether the domain has been set to be long enough in the spanwise direction.

$$R_{u'u'}(\Delta z) = \frac{\overline{u'(z)u'(z + \Delta z)}}{\overline{u'(\Delta z)u'(\Delta z)}} \tag{1}$$

Fig. 9 shows flow immediately transitioning to $3D$ once it reaches the aerofoil upper surface. For $\alpha = 9°$, u' and v' show a strong correlation over $x/c \leq 0.1$ [Fig. 9(I)]. This point is still within the re-circulation bubble [Fig. 4(a)]. This strong correlation relaxes for v' after the bubble at $x/c = 0.2$ but remains very much the same for u' at about 80%. This suggests that for $\alpha = 9°$ over the $x/c \leq 0.2$ the flow has not yet completely transitioned to turbulence. The strong correlation for u' could also indicate existence of large-scale, low frequency structures over the span. This would mean that the spanwise length $L_z = c$ is not wide enough, and further investigation is required. On the other hand, the correlation for w' [Fig. 4(a)] suggests that the flow becomes 3D shortly after the LE with small scale fluctuations in w'. This is consistent with the distribution of the spanwise wall shear stress depicted in Fig. 3(a). In fact, there is a very low magnitude positive/negative alternation of τ_{zz} patches within the bubble region. Note that despite the existence of such three-dimensionality, the flow appears to be dominantly 2D, as inferred from correlations of u' and v'. The w' behaviour is very similar at all locations for
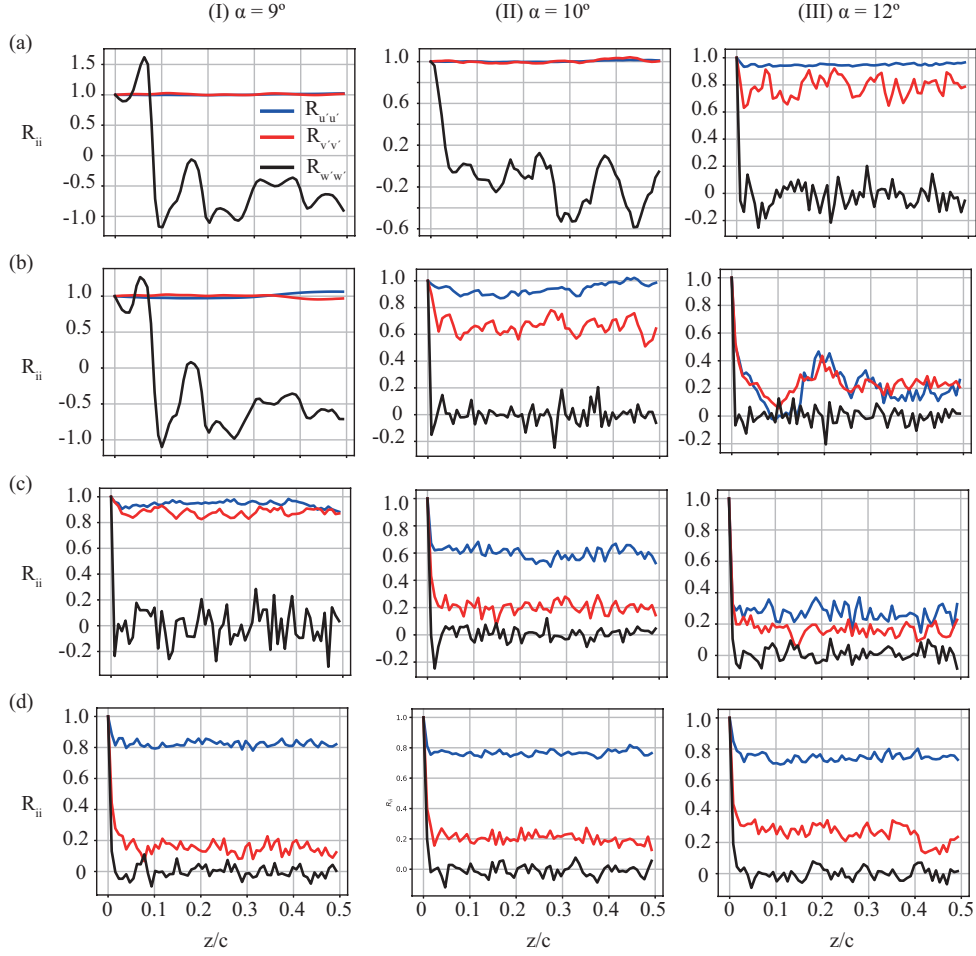
7

Figure 9: Correlation of fluctuating velocities at angles of attack $\alpha = 9°$, $10°$ and $12°$ at several locations along the chord. (a) $x/c = 0.046$ (b) $x/c = 0.061$ (c) $x/c = 0.1$ (d) $x/c = 0.2$.

the remaining angles of attack. However, as the angle increases to $\alpha = 10°$, the v' correlation weakens to 60% at $x/c = 0.061$ and further reduces 0.2 at $x/c = 0.1$. This is accompanied by a reduction in correlation for u' over the span up to $x/c = 0.1$. This suggest the existence of a large scale structure breaking down. For $\alpha = 12°$ we have a similar behaviour and the flow becomes fully 3D after we pass the bubble at $x/c = 0.1$. It should be noted, however, that the fluctuating axial velocity correlation recovers to relatively high values (0.8) at 20% chord. The true nature of such behaviour is still not fully clear to us and is under further investigation.

3.2 Turbulent Transition

To be able to asses where the turbulent transition occurs, the typical boundary layer integral quantities were calculated. These integral quantities are the displacement thickness δ^* [Eq.(2a)], momentum thickness θ [Eq.(2b)] and the shape factor H [Eq.(2c)]. Note that $u_{Ref}(x)$ in Eq.(2) is the reference velocity magnitude at the detected δ_{99} location.
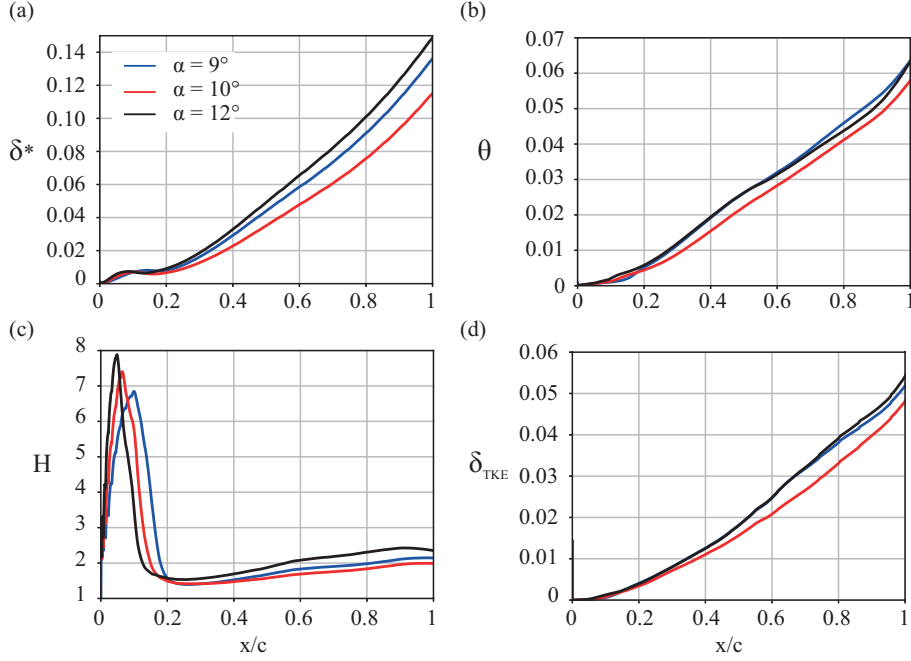
Figure 10: Boundary layer related profiles. (a) Displacement thickness δ^* (b) Momentum thickness θ (c) Shape factor H (d) Blackwelder parameter δ_{TKE}.

$$\delta^* = \int_0^{\delta_{99}(x)} \left(1 - \frac{u(x,y)}{u_{Ref}(x)}\right) dy \tag{2a}$$

$$\theta = \int_0^{\delta_{99}(x)} \frac{u(x,y)}{u_{Ref}(x)} \left(1 - \frac{u(x,y)}{u_{Ref}(x)}\right) dy \tag{2b}$$

$$H = \frac{\delta^*}{\theta} \tag{2c}$$

Further, the *Blackwelder parameter* (δ_{TKE}) was also computed and this is defined as the integral over the boundary layer height of the diagonal *Reynolds stresses* components[1]:

$$\delta_{TKE} = \frac{1}{u_{Ref}^2(x)} \int_0^{\delta_{99}(x)} \left(\frac{\overline{u'u'} + \overline{v'v'}}{2}\right) dy \tag{3}$$

These boundary layer quantities are all reported in Fig. 10. Both displacement thickness δ^* [Fig. 10(a)] and momentum thickness θ [Fig. 10(b)] confirm what we have already observed for the boundary layer thickness δ_{99} in Fig. 6(a). The momentum thickness θ is very close for $\alpha = 9°$ and $\alpha = 12°$ while for $\alpha = 10°$, the θ profile lies distinctly under that of the other two. The same trend is evident for δ^*, however $\delta^*_{\alpha=9°}$ is now clearly lower than $\delta^*_{\alpha=12°}$ with $\delta^*_{\alpha=10°}$ distinctly placed below the other trends [Fig. 10(a)]. Such behaviour for $\delta^*_{\alpha=10°}$ could be related to some flow instability occurring over the aerofoil chord length at $\alpha = 10°$, as this angle of

---

[1]including the w' component made no change to the trend, only to the magnitude.
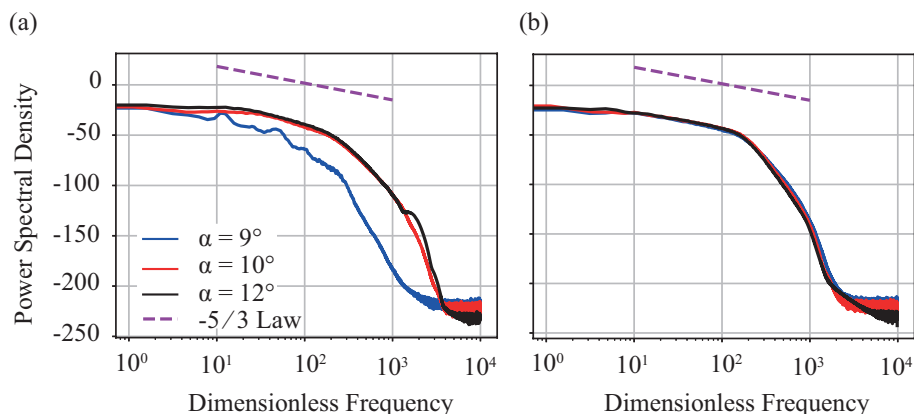
Figure 11: Power Spectral Density of fluctuating axial velocity at (a) $x/c = 0.1$ (b) $x/c = 0.2$

attack corresponds to the maximum lift. However, its true nature is not clear to us at this point in time and is under further investigation.

The shape factor H [Fig. 10(c)] clearly shows that the separation occurs immediately, however the size of the bubble and transition region significantly reduces as the angle of attack is increased. This is again consistent with our previous analysis.

A final point concerning these integral quantities concerns the *Blackwelder* parameter as shown in Fig. 10(d). This measures the fluctuating velocity quantities and it therefore provides an indication as to where the flow is turbulent. For all cases, this point occurs before the 10% chord length. After this, the trend smoothly increases, showing a similar behaviour to δ^* and θ. Another quantity giving a more precise indication as to whether the flow has transitioned or not is the *PSD* of the fluctuating axial velocity (measured at $x/c = 0.1$ and $x/c = 0.2$). This is reported in Fig. 11. At $10^{\%}$ chord, the $\alpha = 10°$ and $\alpha = 12°$ cases show the flow to be fully turbulent, with the $-\frac{5}{3}$ decay visible in a limited band of frequencies. On the other hand the lowest angle of attack $\alpha = 9°$ still shows a higher slope with a couple of frequency peaks. At 20% chord length, the spectral range following the turbulent decay rate is wider and identical for all cases. Of note is the aggressive decay in the *PSD* at higher frequencies: these are the unresolved small length-scales and would required a finer mesh or higher polynomial order to be properly captured.

4 CONCLUSIONS & FUTURE WORK

In this work, a high-order *spectral-h/p element* incompressible *Navier-Stokes* solver belonging to the Nektar++ suite of codes was employed. A preliminary study of the flow behaviour around a *NACA*0012 at various various high angles of attack and an intermediate *Re* of 1.5×10^5 has been presented. Simulations were performed using an *implicit LES* formulation resolving turbulent structures. Our results indicate that even at a pre-stall angle of attack ($\alpha = 9°$) the flow separates near the *LE*. For all three angles considered in this work, the separation is accompanied by a laminar separation bubble with a re-circulation flow inside. The width of the bubble decreases while its height increases as the aerofoil is tilted further. The correlations of

fluctuating velocities suggest the existence of a long (in the spanwise direction) low frequency structure, larger than the chord length of our simulations. Turbulent boundary layer height and corresponding integral quantities, such as displacement and momentum thickness, show a decrease with the angle of attack corresponding to the maximum lift at $\alpha = 10°$. This behaviour is currently being analysed to find its root cause. Analysis of the frequency spectrum within the bubble region indicated the presence of fairly wide-band peaks in the fluctuating velocity. The turbulent transition region also moves upstream as α is increased. In fact, for the lowest angle-of-attack, the flow did not fully transition till after the 10% plate length mark. However, all cases showed fully turbulent behaviour at the 20% chord point. Further work is ongoing to gain the appropriate understanding of the complex flow physics of this case, such as the boundary layer height changes and the presence of spanwise large scale low-frequency structures.

Acknowledgement

References

[1] S. Eftekhari, A. S. M. Al-Obaidi, Investigation of a naca0012 finite wing aerodynamics at low reynold's numbers and 0º to 90º angle of attack, Journal of Aerospace Technology and Management 11 (2019).

[2] S. Martínez-Aranda, A. García-González, L. Parras, J. Velázquez-Navarro, C. Del Pino, Comparison of the aerodynamic characteristics of the naca0012 airfoil at low-to-moderate reynolds numbers for any aspect ratio, International Journal of Aerospace Sciences 4 (2016) 1–8.

[3] M. Y. Zakaria, M. M. Ibrahim, S. Ragab, M. R. Hajj, A computational study of vortex shedding from a naca-0012 airfoil at high angles of attack, International Journal of Aerodynamics 6 (2018) 1–17.

[4] E. Eljack, J. Soria, Y. Elawad, T. Ohtake, Simulation and characterization of the laminar separation bubble over a naca-0012 airfoil as a function of angle of attack, Physical Review Fluids 6 (2021) 034701.

[5] M. E. Rosti, M. Omidyeganeh, A. Pinelli, Direct numerical simulation of the flow around an aerofoil in ramp-up motion, Physics of Fluids 28 (2016) 025106.

[6] A. Poels, X. Collin, A. Benaissa, D. Poirel, Mode and regime identification for a static naca0012 airfoil at transitional reynolds numbers, Mechanics & Industry 21 (2020) 620.

[7] C. Geuzaine, J.-F. Remacle, Gmsh: A 3-d finite element mesh generator with built-in pre- and post-processing facilities, International journal for numerical methods in engineering 79 (2009) 1309–1331.

[8] C. D. Cantwell, D. Moxey, A. Comerford, A. Bolis, G. Rocco, G. Mengaldo, D. De Grazia, S. Yakovlev, J.-E. Lombard, D. Ekelschot, et al., Nektar++: An open-source spectral/hp element framework, Computer physics communications 192 (2015) 205–219.

[9] D. Moxey, C. D. Cantwell, Y. Bao, A. Cassinelli, G. Castiglioni, S. Chun, E. Juda, E. Kazemi, K. Lackhove, J. Marcon, et al., Nektar++: Enhancing the capability and application of high-fidelity spectral/hp element methods, Computer Physics Communications 249 (2020) 107110.

[10] G. Karniadakis, Spectral element-fourier methods for incompressible turbulent flows, Computer Methods in Applied Mechanics and Engineering 80 (1990) 367–380.

[11] G. E. Karniadakis, M. Israeli, S. A. Orszag, High-order splitting methods for the incompressible navier-stokes equations, Journal of computational physics 97 (1991) 414–443.

[12] R. C. Moura, A. Cassinelli, A. F. da Silva, E. Burman, S. J. Sherwin, Gradient jump penalty stabilisation of spectral/hp element discretisation for under-resolved turbulence simulations, Computer Methods in Applied Mechanics and Engineering 388 (2022) 114200.

[13] G. Karniadakis, S. Sherwin, Spectral/hp element methods for computational fluid dynamics, Oxford University Press, 2013.

[14] K. P. Griffin, L. Fu, P. Moin, General method for determining the boundary layer thickness in nonequilibrium flows, Physical Review Fluids 6 (2021) 024608.